Atomic-Scale Observation of the Ni Activation Process for Partial Oxidation of Methane Using In Situ Environmental TEM

ARTICLE *in* CHEMCATCHEM · JUNE 2011

Impact Factor: 4.56 · DOI: 10.1002/cctc.201000238

3 AUTHORS, INCLUDING:

Ritubarna Banerjee
University of South Carolina
6 PUBLICATIONS **45** CITATIONS

SEE PROFILE

DOI: 10.1002/cctc.201000238

Atomic-Scale Observation of the Ni Activation Process for Partial Oxidation of Methane Using In Situ Environmental TEM

Santhosh Chenna, Ritubarna Banerjee, and Peter A. Crozier*[a]

■■please insert the academic titles of the authors■■In situ environmental transmission electron microscopy (ETEM) studies on nanostructures, in parallel with conversion and selectivity measurements, have been carried out on Ni/SiO_2 catalysts for partial oxidation of methane, in order to elucidate structure–property relationships. In situ ETEM experiments under different gas conditions are carried out to simulate the various gas atmospheres that exist in the ex situ reactor. During ramp-up in CH_4 and O_2, Ni metal particles transform to void-like NiO particles at temperatures above 300 °C due to preferential migration of Ni cations along grain boundaries and extended defects. As the temperature increases, the gas environment becomes more reducing, transforming NiO back to Ni and favoring syngas formation. The NiO reduction mechanism also involves diffusion of Ni cations along grain boundaries and extended defects. This transformation pathway suppresses the formation Ni metal crystallites on the catalyst surface during the early stage in NiO reduction. Syngas formation only takes place during the later stages of NiO reduction, when Ni metal nanoparticles have broken through the NiO shell.

Introduction

Understanding structure–property relations for heterogeneous catalysts is essential in developing a complete fundamental understanding of the functionality of catalytic materials. Although ex situ electron microscopy provides significant information on the catalyst structure and composition, the observations may not be representative of the catalyst in its working state. A fresh catalyst may undergo significant changes during a reaction, such as phase transformations, shape changes etc.,) based on the surrounding gas environment. A major challenge in catalyst characterization is developing methods that allow catalytic materials to be studied at the high temperatures and pressures that typically exist in reactors. In situ environmental transmission electron microscopy (ETEM) allows materials to be studied under reactive gas conditions and is ideally suited for studying the high-surface-area nanomaterials that are often employed as catalysts. Starting with the early pioneering work of Baker[1], many groups have shown the power of ETEM for studying dynamic gas–solid reactions in catalytic materials (see Refs.[2–12]). Most of the current instruments operate at pressures of a few torr (1 torr = 133.32 Pa■■SI units. ok?■■) and temperatures up to 800 °C. Recent work has demonstrated that the technique can be further developed to allow catalysts to be studied at pressures up to one atmosphere (1 atm = 101 325 Pa■■SI units. ok?■■).[13]

We have applied ETEM to monitor the evolution of materials that takes place during the initial activation of model Ni catalysts for partial oxidation of methane. Partial oxidation of methane (POM), is an important reaction for syngas production because of its slight exothermic nature,[14–16] and the product gas ratio ($H_2/CO = 2$) obtained is suitable as input for Fischer–Tropsch synthesis.[17,18] POM may also be useful for other energy-related processes, such as fuel reforming for high-temperature fuel-cell applications.[19] Noble metals are very efficient and stable for converting methane to syngas,[14,15,17,18,20,21] with Ru and Rh being among the fastest for reaching thermodynamic equilibrium conversions. However, noble metals are costly for large-scale applications. Supported Ni catalysts have also been studied as less expensive options for partial oxidation of methane. Ni catalysts have shown high conversion efficiencies at low cost,[14–16] although deactivation by coke formation and sintering can be problematic.

The catalyst structure and composition must be determined under so-called "reactor conditions," which necessitates observation of the material under suitable temperatures and ambient gas conditions. The structures observed can then be correlated to catalyst activity determined under similar conditions, so that structure–property relations can be determined. However, establishing these correlations with ETEM is not straightforward because of the very significant differences between the ETEM reactor and the ex situ reactor employed to measure catalytic properties.

For partial oxidation of methane under high conversion conditions, the gas composition in the reactor changes along the catalyst bed from 100% reactant gas at the entrance of the bed to close to 100% product gas at the exit, with intermediate gas products in the middle. The gas composition across the reactor is influenced by the reaction pathway for syngas formation. Two main reaction mechanisms have been proposed for the POM reaction [Eq. (1)]. One is the indirect POM,

[a] S. Chenna, R. Banerjee, P. A. Crozier
School for Engineering of Matter, Transport and Energy
Arizona State University, Tempe, AZ 85287-6106 (USA)
Fax: (+1) 480-727-9321
E-mail: crozier@asu.edu

where the reaction proceeds through complete combustion of methane to CO_2 and H_2O [Eq. (2)] followed by carbon dioxide and steam reforming [Eq. (3) and (4)].[22,23] The other is direct POM to syngas without the formation of CO_2 and H_2O.

$$CH_4 + {}^1/_2O_2 \rightarrow CO + 2H_2 \quad \Delta H^\circ_{298} = -36\ kJ\ mol^{-1} \quad (1)$$

$$CH_4 + 2O_2 \rightarrow CO_2 + 2H_2O \quad \Delta H^\circ_{298} = -802\ kJ\ mol^{-1} \quad (2)$$

$$CH_4 + CO_2 \rightarrow 2CO + 2H_2 \quad \Delta H^\circ_{298} = +247\ kJ\ mol^{-1} \quad (3)$$

$$CH_4 + H_2O \rightarrow CO + 3H_2 \quad \Delta H^\circ_{298} = +206\ kJ\ mol^{-1} \quad (4)$$

Most experimental findings support the indirect POM reaction pathway on Ni catalysts.[21] Thus the gas compositions present in the reactor will involve mixtures of CH_4, O_2, CO_2, CO, H_2O, and H_2, with the exact composition depending on the location and temperature on the reactor bed. Moreover, during the reactor ramp-up, the catalyst structure and activity will change with temperature leading to further changes in the ambient gas composition. Thus during ramp-up, the "reactor condition" varies in time and space and it is important to take this into account in the design and interpretation of ETEM experiments.

A further challenge relates to the inherent complexity that is often present in the nanostructure and composition of real working catalysts. Even under ex situ conditions, many "simple" heterogeneous catalysts show a variety of structures and morphologies between and within individual nanograins. Many common high-surface-area supports may be composed of nanocrystals with multiple crystal facets and complex surface defect structures. For example, in our previous work on Ni supported on TiO_2, we found that the nature of the metal–support interaction depended on whether the metal nucleated on anatase or rutile grains and on the particular crystal facet of these two different titanias.[24,25] The complexity of high-surface-area support structures can lead to significant heterogeneity in the microstructure of supported monometallic catalyst and provide rich but complex nanostructure in bimetallic systems.[8,9] For in situ work in which dynamic structural changes take place during reaction conditions, this structural complexity greatly complicates the interpretation of the TEM data. For this reason, we have chosen to work on a simple model system consisting of Ni nanoparticles supported on SiO_2 spheres. Unlike the other oxide supports like Al_2O_3 and TiO_2, where Ni metal interact strongly with the support forming $NiAl_2O_4$ and $NiTiO_3$ respectively,[21] the surface of the SiO_2 spheres is relatively homogenous and interacts only weakly with the Ni particles. Moreover the simple geometry of this support is ideal for observing and interpreting changes in metal particle size, shape, and composition during in situ ETEM studies.

Results and Discussion

Ni/SiO_2 Catalyst Performance

SiO_2 spheres were prepared using Stober's method and employed as the oxide support. Ni/SiO_2 catalysts with Ni loadings of 2.5 and 7.3 wt% were prepared using an incipient wetness technique with nickel nitrate hexahydrate as precursor. The activity and selectivity of the catalysts for partial oxidation of methane were determined with an In Situ Research Instruments RIG 150 reactor containing a quartz tubular fixed-bed flow furnace. The catalyst was initially reduced at 400 °C in 5% H_2/Ar for 2 h to remove any oxide layer formed due to air exposure. Reactions were typically performed using a feed mixture of $CH_4/O_2/He = 8:4:50$. Figure 1 shows the conversions of

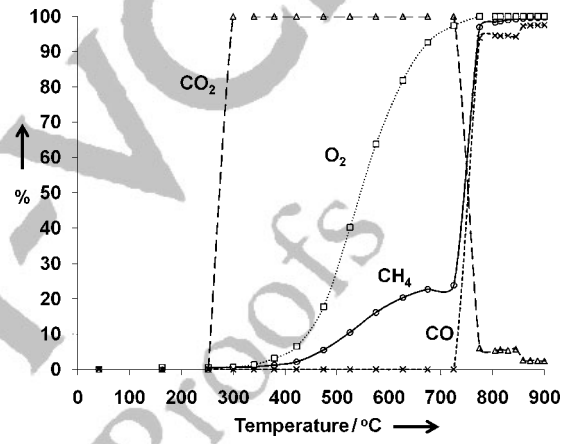

Figure 1. Conversion and selectivity for partial oxidation of methane over a model 2.5 wt% Ni/SiO_2 catalyst.

CH_4 and O_2 and selectivity for CO_2 and CO on a 2.5 wt% catalyst during POM. During the temperature ramp-up, negligible conversion of CH_4 takes place at temperatures below 300 °C. Complete combustion of up to 24% of CH_4 takes place in the temperature range of 300–750 °C, as demonstrated by the CO_2 formation and the near 100% O_2 conversion at 750 °C. A further increase in temperature to 775 °C resulted in a sudden increase in CH_4 conversion from 24% to 97% with almost all CH_4 being converted to CO and H_2. Slight increases in CH_4 conversion and CO selectivity were observed with a further stepwise increase in temperature to 900 °C. The 7.3 wt% sample showed similar trends but the main rise in CH_4 conversion was shifted to higher temperature.

Figure 2 illustrates the possible variation in gas composition along the catalyst bed for three different temperature regimes. The catalyst bed was divided into three regions (not necessarily equal). At temperatures below 300 °C, all regions of the bed are exposed to a mixture of CH_4 and O_2 (2:1). In the temperature range of 300–750 °C, at region 1, ■■Roman numerals replaced in accordance with journal style. ok?■■ at the front of the bed, the reactant mixture consists mostly of CH_4 and O_2, ■■ok?■■ whereas regions 2 and 3 are exposed to mixtures containing CH_4, O_2, CO_2, and H_2O. With increasing temperature,

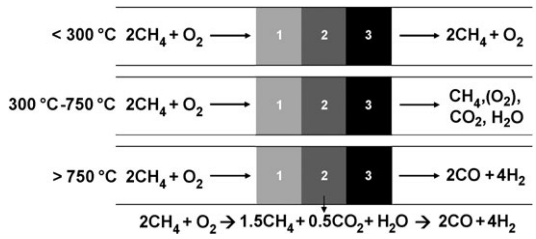

Figure 2. Variations in the gas composition along the catalyst bed (regions 1, 2, and 3) over different temperature ranges.

the CO_2 and H_2O concentrations increase in regions 2 and 3 of the bed, with consumption of CH_4 and O_2. Above 750 °C, region 2 is exposed mostly to a mixture of CH_4, CO_2, and H_2O, because most of the O_2 is consumed during complete combustion of CH_4 in region 1. Reforming of methane with CO_2 and H_2O takes place in region 2 and region 3 is exposed mostly to a mixture of CO and H_2 (1:2). In reality, there is a continuous change in the gas composition across the bed and Figure 2 simply illustrates the dominant compositions present at different locations and temperatures, to facilitate the design of appropriate ETEM experiments.

Initial Stage of Ramp-Up: NiO Voids and Complete Oxidation of Methane

ETEM was performed on an FEI Tecnai F20 under gas pressures of about 133 Pa. The amount of catalyst present in the ETEM was very small (< 1 μg)■■ok?■■, whereas the volume of the cell in the ETEM was 1000 cm^3 with a flow rate at 133 Pa of about 300 mL min^{-1}. Under these conditions, in contrast to the ex situ reactor, there is negligible conversion of reactants to products and the gas composition throughout the cell will be dominated by the inlet gas composition. The samples were reduced in situ in the presence of H_2 at 400 °C before exposing them to the various gas mixtures of relevance for partial oxidation of methane. Typical Ni metal particle sizes were determined by TEM for the 2.5 and 7.3 wt% Ni samples after in situ reduction (Figure 3). The 2.5 wt% sample had an average particles size of about 5.5 nm with 80% of the particles within the range 3–10 nm. For the 7.3 wt% sample, the average particle size was also 5.5 nm, but only 50% of the particles were within the range 3–10 nm.

To investigate the structure of the catalysts at different points along the reactor bed at different temperatures, a series of ETEM experiments were undertaken in gas mixtures corresponding to the various gas compositions shown in Figure 2. The ETEM conditions were labeled A–H and are defined in Table 1. Conditions A and B were always run in sequence at the beginning of each experiment to mimic the initial start-up procedures in the RIG 150 reactor (i.e. experiments exploring conditions C to H are always preceded by A and B). The gases for each experiment were pre-mixed in a mixing tank in the desired ratios before admission into the cell. In situ reactions were carried out at pressures of 40–107 Pa■■SI units. ok?■■. Electron beam damage effects were characterized and avoided by employing low-dose imaging techniques during catalyst observation along with beam blanking during the ramp-up and waiting periods.

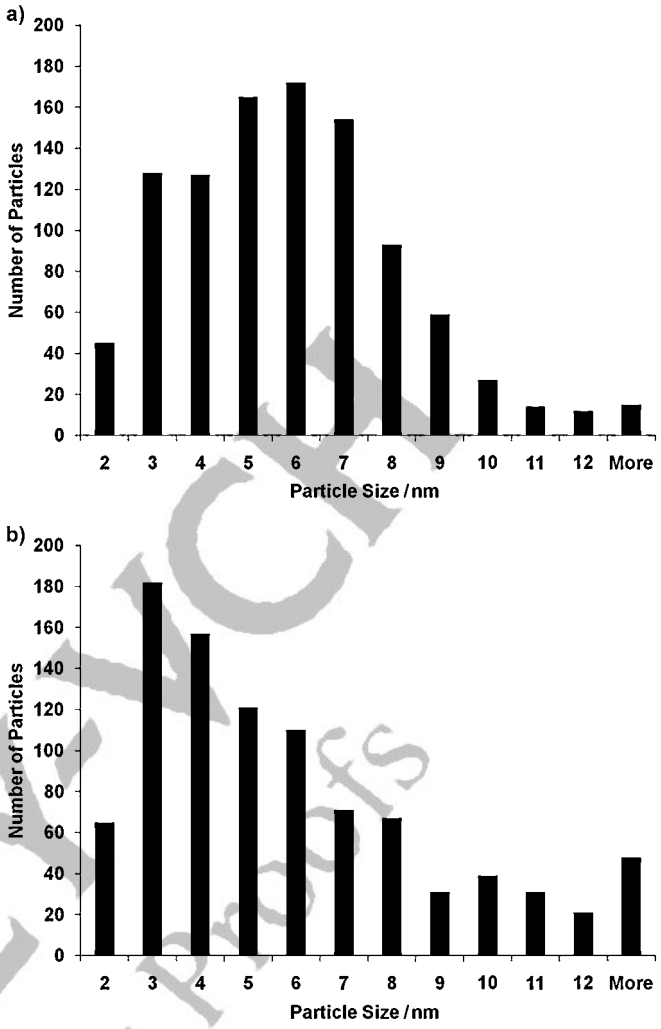

Figure 3. Ni particle size distributions: a) 2.5 wt% metal loading; b) 7.3 wt% metal loading on SiO_2 support.

Table 1. Experimental conditions showing the gas environments, reaction temperatures and reaction times used during the in situ ETEM studies.

Condition	Gas Environment	T [°C]	t [h]
A	H_2	400	2
B	$2CH_4+O_2$	400	1
C	$2CH_4+O_2$	800	2
D	$CO+2H_2$	400	3
E	$CO+2H_2$	800	3
F	$3CH_4+CO_2+2H_2O$	400–700	3
G	CH_4	700	1
H	CH_4	500	3

Figure 4a shows a typical in situ ETEM image and electron diffraction pattern of Ni/SiO_2 in the presence of 107 Pa of H_2 at 400 °C (condition A). Ni particles are mostly de-wetting the SiO_2 surface and the diffraction pattern confirms that the particles are fcc nickel metal. Figure 4b shows the same area in the

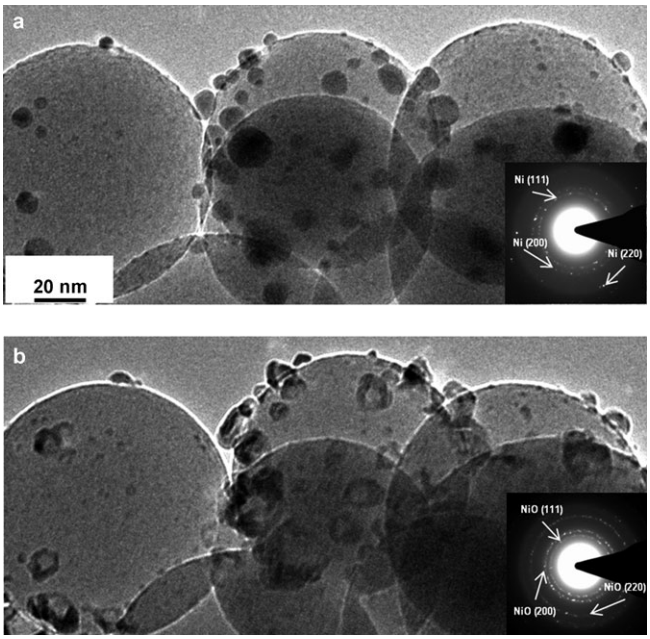

Figure 4. In situ ETEM images and electron diffraction patterns of Ni/SiO_2: a) In presence of 107 Pa■■SI units. ok?■■ of H_2 at 400 °C (condition A); b) from the same region in presence of 107 Pa of mixture of CH_4 and O_2 in 2:1 ratio at 400 °C (condition B).

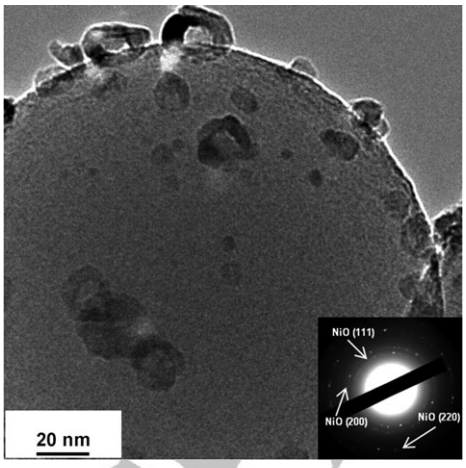

Figure 5. Ex situ TEM image and electron diffraction of Ni/SiO_2 after ramping to 400 °C in CH_4 and O_2 and then cooling to room temperature in flowing He.

presence of 107 Pa of a 2:1 mixture CH_4 and O_2 at 400 °C (condition B). The larger Ni nanoparticles have transformed to a structure showing a void-like morphology that partially wets the SiO_2 surface. No voids were observed on NiO nanoparticles of sizes below 5 nm. Electron diffraction shows the nanoparticles are now fcc NiO. These void structures, which start to form at about 300 °C, were initially surprising because we had not observed such morphology on the used catalyst. However, this observation was reproduced in repeated runs in the electron microscope.

As a further check on the validity of the in situ observations, we analyzed several samples from the ex situ reactor at an equivalent point in the ramp-up. After the initial reduction step, the catalyst was heated to 400 °C in the ex situ reactor in the presence of CH_4 and O_2 in a 2:1 ratio. The sample was then cooled to room temperature and immediately transferred into a TEM for observation. Figure 5 shows a typical image and diffraction pattern from the ex situ sample and confirms both the formation of the void structured morphology and the complete conversion of the Ni to fcc NiO. This finding indicates that the void structure is an intermediate phase formed in the catalyst during ramp-up. Nanoparticle evolution was monitored in the presence of the CH_4 and O_2 mixture up to 800 °C (condition C) and the diffraction pattern confirms Ni exists as NiO even at this high temperature.

In the ETEM experiment, the phase transformation of Ni to NiO is due the high partial pressure of O_2 (ca. 36 Pa) in the gas flow. In the ex situ reactor, the catalyst bed is also exposed to a high oxygen partial pressure at temperatures up to 700 °C. At these oxygen pressures, there is a strong thermodynamic driving force for oxide formation.[27] The presence of the reducing agent CH_4 does not significantly affect the phase transformation because of the higher chemisorption energy of O_2 on the Ni surface compared to CH_4; chemisorption energies for the Ni(111) surface are 481 kJ mol^{-1} for the O adatom and 192.28 kJ mol^{-1} for CH_3^- adsorption.[28,29] Consequently, the surface is mostly covered by O adatoms, favoring initial NiO formation kinetically as well as thermodynamically.

After the initial oxidation of the surface, the Ni metal particle is surrounded by an oxide shell and there are two possible mechanisms for the particle oxidation process to continue. O anions can diffuse through the oxide shell to the metal below or metal cations can diffuse through the oxide layer and interact with O on the surface of the NiO. The dominant mechanism will depend on the relative magnitudes of the diffusion coefficients for O and Ni diffusing in NiO. A clue to the mechanism for oxidation and void formation is that the void has a similar size to the initial Ni particle (Figure 6c), which shows a colorized superposition of the NiO image (Figure 6b) and the Ni metal image (Figure 6a). These images suggests a Kirkendall-type process,[30] in which the Ni cations diffuse through the NiO shell.

An analysis of published diffusion coefficients in this case shows that coefficients for species diffusing along the grain boundary are many orders of magnitude higher than those for diffusion through the perfect crystal■■ok?■■. Furthermore, the coefficient for Ni diffusion along grain boundaries and line defects in NiO is eight orders of magnitude higher that the corresponding O coefficient (10^{-13} cm^2 s^{-1} and 10^{-21} cm^2 s^{-1} at 400 °C for Ni and O respectively).[31–33] Figure 7 shows an atomic-resolution image of a typical NiO particle in the presence of CH_4 and O_2 at 400 °C. The image shows many grain boundaries and extended defects on the NiO particle, caused by simultaneous growth of distinct nuclei of NiO on the surface of the Ni particles. Thus the grain boundaries between adjacent NiO nuclei act as rapid diffusion paths for subsequent migration of Ni to the particle surface. Diffusion of Ni through NiO creates vacancies inside the metal particle, which migrate

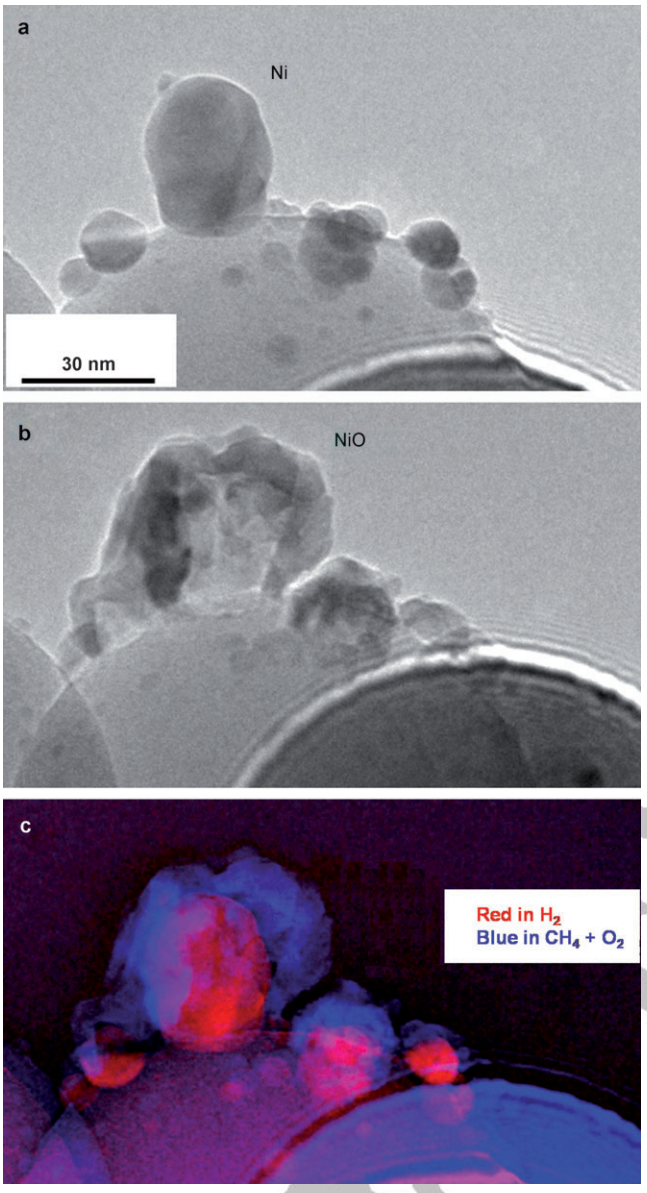

Figure 6. In situ ETEM images of Ni/SiO_2: a) In presence of 107 Pa■■SI units. ok?■■ of H_2 at 400 °C; b) from the same region in presence of 107 Pa of mixture of CH_4 and O_2 in 2:1 ratio at 400 °C; c) superposition of colorized images shown in (a) and (b).

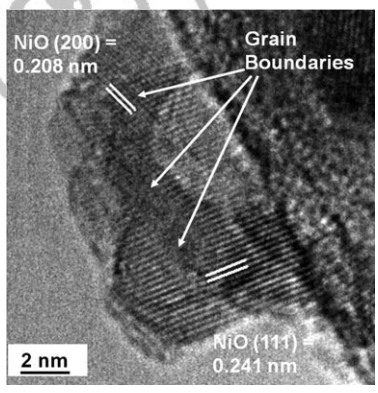

Figure 7. In situ high-resolution ETEM image of void-structured NiO/SiO_2 in presence of 107 Pa of mixture of CH_4 and O_2 in 2:1 ratio at 400 °C.

towards the metal/SiO_2 interface and coalesce to form a void (Figure 8). Similar morphologies have been reported by Railsback et al. and by Nakumara et al. in studies of the oxidation behavior of Ni nanoparticles in the presence of pure oxygen.[34,35]

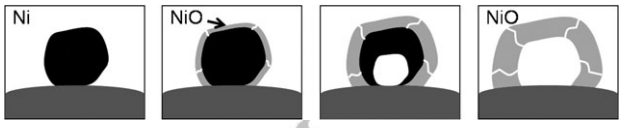

Figure 8. NiO void formation by Kirkendall effect.

Smaller Ni particles (< 4 nm) do not seem to undergo oxidation by this mechanism. For these particles, the diffusion distances are very short and it becomes kinetically possible for the oxide particles to achieve their thermodynamic equilibrium shape of a solid particle. (The void morphology is not the equilibrium shape because of the larger total surface energy associated with the internal surface of the void). In this particular case, these smaller particles represent a minor component of the surface area associated with the catalyst. From the particle size distributions (Figure 3a,b), the total fraction of surface area associated with Ni particles of different size can be determined simply by assuming that each particle is a sphere (a good approximation in this case). This analysis (Figure 9) shows that the percentage of surface area associated with particle sizes less than 4 nm is 7% and 8% for 2.5 wt% and 7.3 wt% loadings, respectively. Thus for these particular model catalysts, the oxidation and reduction mechanisms associated with the larger particles dominate the overall catalytic activity.

Final Stage of Ramp-up: Ni Particle and Syngas Formation

NiO is not an active phase for syngas production. For syngas production, Ni metal must be present on the surface so the NiO must eventually transform back to Ni metal at some later point in the ramp-up process. From the reactor data, as the temperature increases, the gas mixture in regions 2 and 3 of the catalyst bed becomes more reducing as O_2 is consumed. Eventually it becomes thermodynamically favorable for the oxide to transform back to metal and, at this point, the surface of the oxide starts to reduce■■become reduced?■■.

To study the reduction process, in situ experiments were carried out to determine the structure of the nanoparticles during the initial and intermediate stage of reduction under different gas conditions (Table 1). In the strong reducing gas mixture of CO and H_2 at 400 °C (condition D), core–shell structures with dark cores were observed at the intermediate stage of reduction. Diffraction patterns showed that the nanoparticles contained both NiO and Ni metal. When the reduction was performed at temperatures from 400 to 700 °C in the presence of CH_4, CO_2, and H_2O (condition F), a gas mixture corresponding to region 2 of the catalyst bed, diffraction patterns also showed the nanoparticles contained both Ni metal and NiO. Complete reduction of NiO to Ni took place relatively quickly

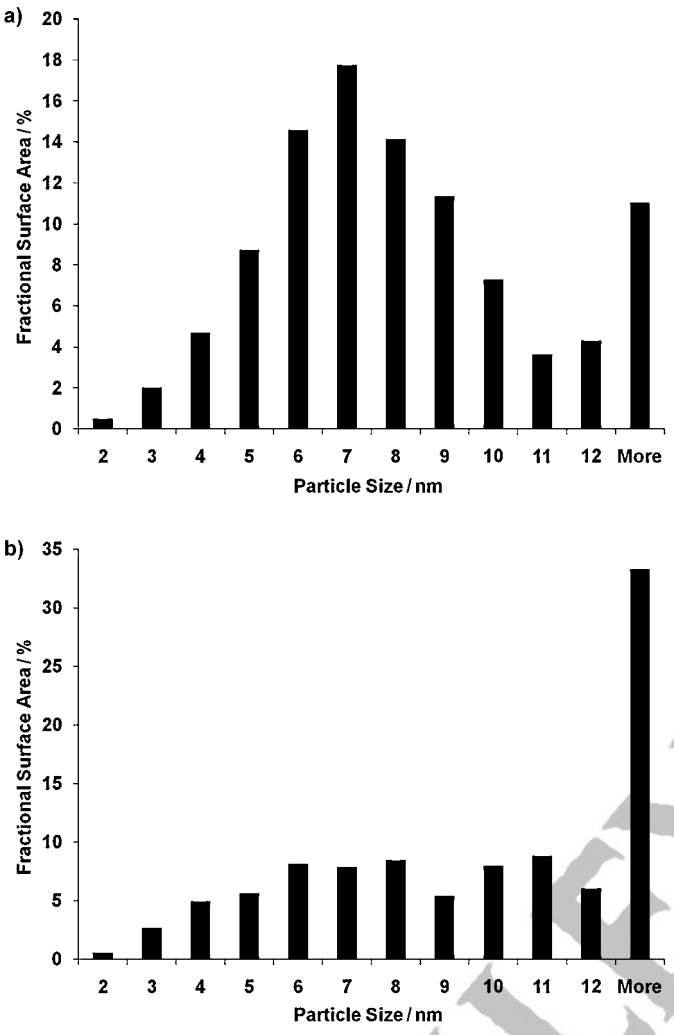

Figure 9. Fractional surface area associated with Ni particles of different sizes: a) 2.5 wt% Ni loading; b) 7.3 wt% Ni loading.

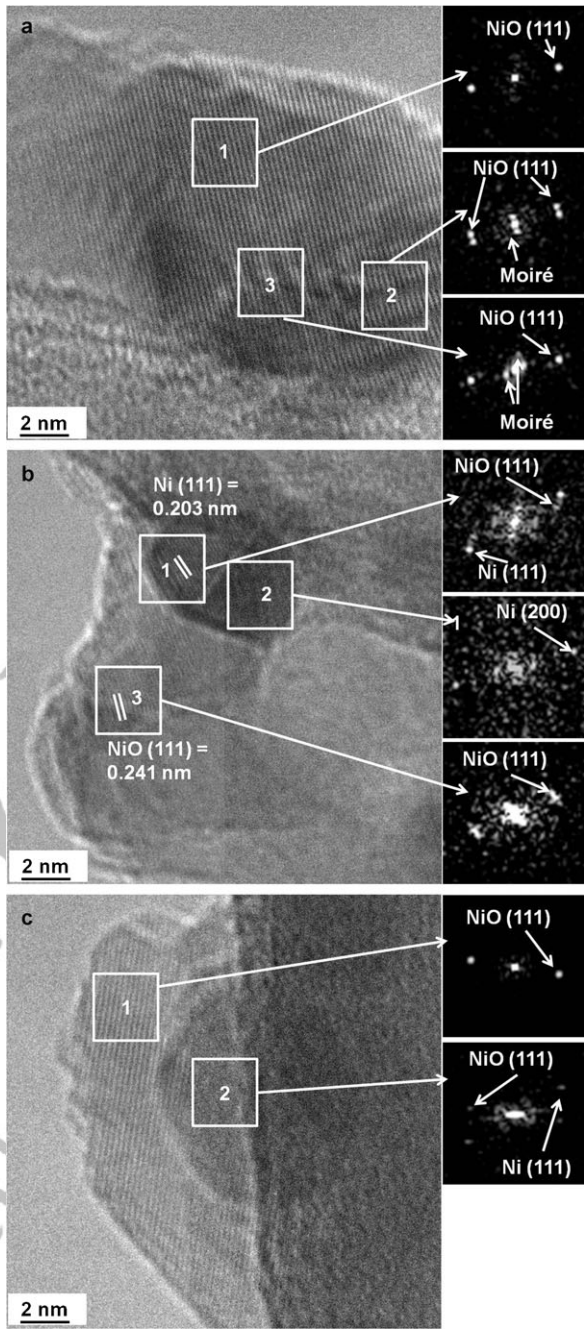

Figure 10. In situ high-resolution ETEM images along with FFTs of Ni/SiO_2 in the presence of 40 Pa■■SI units. ok?■■ of CH_4 at 500 °C at different reduction times: a, b) Initial stages of reduction; c) intermediate stage of reduction.

when heated to 700 °C in the presence of pure CH_4 (conditions G).

In the reduction experiments reported above under a variety of reducing conditions, we never observed the formation of Ni metal shells implying that the primary diffusing species is again Ni cations. To further investigate the reduction mechanism, we conducted additional experiments in CH_4 at relatively low temperature so that the intermediate morphologies could be determined. Figure 10 shows high-resolution images along with their fast-Fourier transforms (FFTs) from particles observed in 40 Pa■■SI units. ok?■■ of CH_4 at 500 °C at different stages of the reduction process. During the early stage of reduction, some regions in the NiO particles may contain Ni nanodomains. If these domains contain crystalline metallic Ni, then a Moiré pattern may be evident in the high-resolution image due to the superposition of lattice fringes from the oxide and the metal (Figure 10a).

The appearance of a Moiré pattern does not prove that Ni metal is present because Moiré patterns can also result from the superposition of two overlapping crystallites of NiO. To correctly interpret the Moiré pattern, it is necessary to analyze the pattern in terms of the two fundamental periodicities. Full details of this procedure can be found in textbooks on TEM and involve expressing the reciprocal lattice vector for the Moiré reflection in terms of the reciprocal lattice vectors of the two fundamental reflections.[36] FFTs were taken from different positions on the nanoparticle (Figure 10a) and the local lattice parameter was determined using the Diffpack module for Gatan's Digital Micrograph software. The FFT from position 1 shows

only one pair of spots with a lattice spacing of 0.241 nm, corresponding to the NiO(111) plane (Figure 10a, inset■■ok?■■). The FFT from position 2 shows two pairs of NiO(111) reflections from different lattice orientations along with the Moiré spacing of 1.486 nm. The Moiré was formed from the interference of two NiO(111) lattices. The FFT from position 3 shows only one pair of fundamental reflections corresponding to NiO(111) and two pairs of Moiré reflections with a spacing of 1.082 nm and 0.6608 nm. In this case, the fundamental reflections can be found by expressing the unknown reciprocal lattice vector in terms of the Moiré and NiO(111) reciprocal lattice vectors. This analysis shows that both Moiré reflections are formed from the interference of NiO(111) with two different Ni(111) lattices oriented at different angles. The Ni(111) reflections do not appear in this image because of loss of resolution due to instabilities associated with the hot stage.

Figure 10b shows an example of a NiO particle with a void structure at a later stage of reduction. In this case, a particle with dark contrast was observed at the interface of NiO and SiO_2. From the FFTs, the surface lattice spacing was found to be 0.241 nm corresponding to the NiO(111), position 3, and the lattice spacings in the dark particle are 0.203 nm and 0.176 nm, corresponding to Ni(111) and Ni(200) respectively. Figure 10c shows the core-shell structure formed at a later stage of the reduction in CH_4. FFT confirms the lattice spacing to be 0.241 nm, corresponding to NiO(111) in the shell region and 0.203 nm corresponding to Ni(111) at the core region, indicating a Ni core with NiO shell during the reduction. As the reduction continues, the NiO shell grows thinner and eventually a the particle consists solely of Ni metal. When metallic nickel has formed on the particle surface, formation of graphite sheets occurs due to methane dissociation.

In the CH_4 atmosphere, the primary thermodynamic driving force is to reduce the entire NiO particle to Ni metal (not just the particle surface). Therefore, oxygen from NiO must be continually present on the particle surface to react with CH_4. After the initial surface reduction of NiO, there are two possible transformation mechanisms for the oxide particle to completely reduce to metal, involving either predominant diffusion of O anions (mechanism 1) or predominant diffusion of metal cations (mechanism 2). Figure 11 represents the morphology of the particles that would form during the reduction process based on these two mechanisms. If O anions were the primary diffusing species (Figure 11a), initially the top layer of the metal oxide would be reduced to form a metal-rich shell. O would continue to diffuse through the metal-rich shell to react on the surface, leaving oxygen vacancies in the oxide core. The reduction process would continue until all the O was consumed, creating a Kirkendall void at the center of the metal particle. For example, low-temperature reduction of PdO results in a Pd metal shell with a void at the center, implying an O anion diffusion mechanism.[6,37] In contrast, if the metal was the primary diffusing species (Figure 11b), cations would diffuse away from the surface along defects and grain boundaries, exposing fresh metal oxide and allowing reduction to continue. In this case, metal–metal oxide core–shell structures would form during the intermediate stage of reduction and eventually the oxide skin would vanish, leaving a solid metal particle. For syngas production, mechanism 1, involving the formation of an intermediate metal shell, may be more desirable, since it would mean that even partially reduced NiO would be active for the reaction.

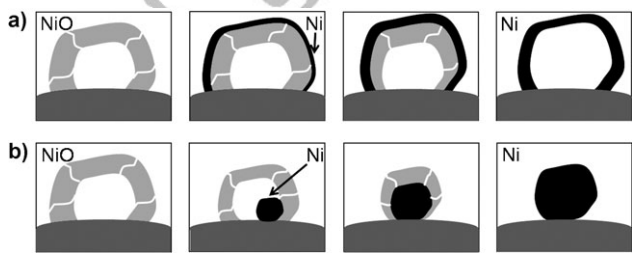

Figure 11. NiO to Ni transformation under two different mechanisms: a) Mechanism 1: O is the dominant diffusing species; b) mechanism 2: Ni is the dominant diffusing species.

Our observations collectively suggest that mechanism 2 is the main process for NiO reduction during ramp-up for POM. This interpretation is further reinforced by comparing the respective diffusion coefficients. The diffusion coefficient of Ni in NiO grain boundaries is approximately $10^{-12}\,cm^2s^{-1}$ at 500 °C[33] and is much greater than the value for O diffusing in Ni metal ($10^{-16}\,cm^2s^{-1}$ at 500 °C[38]). Thus if extended defects that intersect the surface are present in the NiO particles, the reduction to metal will take place according to mechanism 2.

This particle reduction mechanism allows us to interpret the observed sharp increase in syngas production at 775 °C. During the transformation of NiO to Ni, Ni cations rapidly diffuse over the particle surface to extended defect sites and then move to subsurface sites, exposing fresh NiO. TEM images (■■is there a relevant figure?■■) showed that the average distance between grain boundaries and extended defects is on the order of 5 nm. At 500 °C, the diffusion coefficient for Ni diffusing on NiO is about $10^{-11}\,cm^2s^{-1}$ suggesting that Ni species remain on the surface for only a few hundredths of a second. Ni metal crystallites do not form on the surface and the catalyst surface remains predominantly NiO during this process and syngas production is suppressed. Only towards the end of the particle reduction process is there a significant increase in the Ni metal concentration on the surface as growing Ni metal nuclei break through, leading to a concomitant increase in syngas production.

The inactivity of the catalyst below 775 °C is in part caused by difficulty in reducing the metal particle surface, as described above. However, once the catalyst is activated, the reactor temperature can be varied and our measurements (not presented) show the methane conversion and CO selectivity almost match the thermodynamically predicted values. The lack of activity during most of the ramp-up is associated with the undesirable intermediate transformation of Ni metal to NiO. However, if the ramp-up is carried out in a reducing atmosphere, the metal to oxide transformation can be avoided in the downstream region of the bed and thermodynamically limited performance is achieved over an extended temperature range. The experimentally measured CH_4 conversion and CO

selectivity for such an experiment on the same catalyst are shown in Figure 12. In this case, the reactor was ramped to 600 °C in an H_2 flow and then the gas was switched to the CH_4 and O_2 mixture. The catalyst immediately produced syngas with methane conversions near the thermodynamic limit of 60%. With continued ramping, the methane conversion and syngas production continued to increase in accordance with thermodynamic predictions, approaching 99% at 900 °C.[15] The ramp-up procedure ensures that the entire catalyst bed contains only metallic Ni during the H_2 ramp-up to 600 °C. When CH_4 and O_2 are introduced, the Ni metal may initially oxidize, at least in region 1 of the reactor, but at 600 °C this oxide will rapidly convert the gas phase oxygen to CO_2 and H_2O by complete combustion of methane. Thus the oxygen partial pressure in the system will be dramatically lowered across most of the bed under our flow conditions, allowing syngas formation to occur.

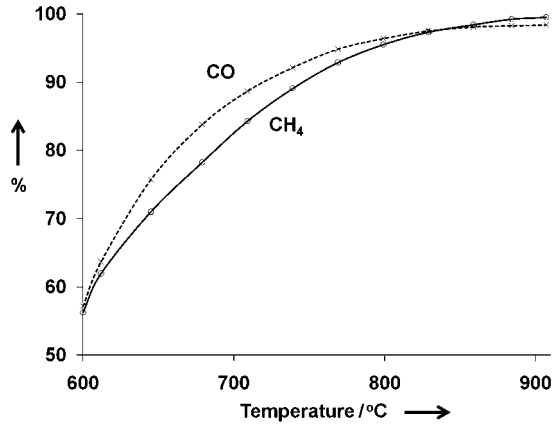

Figure 12. CH_4 conversion and CO selectivity of Ni/SiO_2 catalyst during partial oxidation of methane obtained after H_2 reduction at 600 °C.

Conclusions

In situ ETEM was employed to develop an atomic level description of the structure, composition and morphologies that develop in model Ni/SiO_2 catalyst during ramp-up for partial oxidation of methane under high conversion conditions. The gas composition along the catalyst bed varied in space and time during ramp-up. Essentially there was no single "reactor condition" in this case and the variation in the gas composition had to be taken into account in the design of ETEM experiments so that the correct structure property relations could be determined.

During ramp-up, the Ni metal particles transformed to NiO at about 300 °C in the CH_4 and O_2 reacting gas mixture before any significant catalysis had taken place. The void-like morphology present in NiO nanoparticle greater than 5 nm was due to a Kirkendall process in which Ni cations preferentially diffused along grain boundaries and extended defects in the initial oxide shell. The front of the catalyst bed was exposed in all cases to the reacting gases and the NiO particles present at temperatures above 300 °C favored complete oxidation of CH_4. As the temperature continued to increase, oxygen conversion at the front of the bed increased and the NiO in the later region of the bed transformed back to metallic Ni, leading to syngas formation. ETEM experiments were carried out in a variety of relevant reducing atmospheres and temperatures to investigate the NiO to Ni metal phase transformation. In the CH_4 reducing atmosphere, the NiO reduction mechanism also involved diffusion of Ni cations along grain boundaries and extended defects giving rise to an intermediate catalyst state corresponding to Ni–NiO core–shell structures. This transformation pathway suppresses the formation of Ni metal crystallites on the catalyst surface during the early stage in NiO reduction. Syngas formation would only take place during the later stages of NiO reduction when Ni metal nanoparticles had broken through the NiO shell. This explains the sharp increase in CH_4 conversion and CO selectivity that was observed at 775 °C. Ramping of the catalyst in a reducing atmosphere avoided the syngas delay associated with NiO formation in the latter part of the bed and yielded thermodynamically limited conversion over a wide temperature range.

Experimental Section

Catalyst preparation

2.5 and 7.3 wt% Ni/SiO_2 catalysts were prepared by impregnating SiO_2 spheres with $Ni(NO_3)_2{\cdot}6H_2O$ solution using incipient wetness techniques. SiO_2 spheres were prepared using Stober's method[39] and then calcined at 500 °C for 2 h to remove any precursor residues. Spheres of different sizes were employed with sizes in the range 80–280 nm, determined by TEM. $Ni(NO_3)_2{\cdot}6H_2O$ solution was prepared by dissolving a known amount of 99.999% $Ni(NO_3)_2{\cdot}6H_2O$ (obtained from Sigma Aldrich) using ethanol as a solvent following a method outlined by Banerjee et al.[40] Incipient wetness impregnation was carried out in a mortar by dropwise addition of nickel nitrate solution equivalent to the pore volume of the SiO_2 in a saturated ethanol atmosphere while mixing for 10 min. After impregnation, the sample was dried at 120 °C followed by reduction in 5% H_2/Ar atmosphere at 400 °C for 3 h. The conventional calcination step was avoided to give improved metal dispersions in this case.[41]

Catalytic measurements

The activity and selectivity of the catalyst was determined with an In situ Research Instruments RIG 150 reactor containing a quartz tubular fixed-bed flow furnace with an internal diameter of 10 mm. A K-type thermocouple with a quartz tube was placed at the top of the catalyst bed to measure the temperature of the furnace. The catalyst (10 mg) was loaded into the reactor and initially reduced at 400 °C in 5% H_2/Ar. Reactions were typically performed using a feed mixture of $CH_4/O_2/He = 8:4:50$ with a total flow rate of 62 mL min^{-1}. Partial pressures of CH_4 and O_2 in the gas feed were 13 and 6.5 kPa■■SI units. ok?■■ respectively. A typical run involved ramp-up rates of about 4 °C min^{-1}. The effluent gas from the reactor outlet was analyzed with a Varian 3900 gas chromatography system equipped with two parallel columns of CP-Molsieve 5 A and CP-PoraBOND Q to separate different gases. Both columns

could detect CH_4, O_2, and CO, but CO_2 could be detected only by the CP-PoraBOND Q column. Peak calibration was carried out for different gas compositions before the actual reaction. As He was used as a carrier gas, H_2 was not directly detected; hence CO formation was taken as the reference for measuring the activity of the catalyst for syngas ($CO + H_2$) formation.

In situ ETEM characterization

In situ transmission electron microscopy was performed in an FEI Tecnai F20 field-emission environmental transmission electron microscope (ETEM) operating at 200 kV with a point resolution of 0.24 nm and an information limit of 0.13 nm. The gas reaction cell or environmental cell (essentially a flow microreactor) of this instrument allowed atomic-level observations of gas–solid interactions at pressures up to a few torr■■how many?■■ and temperatures up to 800 °C. In situ electron microscope images and diffraction patterns were recorded with a Gatan CCD camera using Digital Micrograph 3.1 software. The instrument was also equipped with a Gatan imaging filter allowing in situ electron energy-loss spectroscopy to be performed. The catalyst samples were gently crushed between glass microscope slides, loaded onto platinum grids, and placed onto a Gatan Inconel heating holder. The error in determining local sample temperature was +/−25 °C.

Acknowledgements

The support from the National Science Foundation (NSF-CBET-0553445) and the use of TEM at the John M. Cowley Center for High Resolution Microscopy at Arizona State University are gratefully acknowledged.

Keywords: electron microscopy · heterogeneous catalysis · nickel · operando techniques · oxidation

[1] R. T. K. Baker, M. A. Barber, P. S. Harris, F. S. Feates, R. J. White, *J. Catal.* **1972**, *26*, 51.
[2] P. L. Gai, *Top. Catal.* **1999**, *8*, 97.
[3] S. Giorgio, S. Sao Joao, S. Nitsche, D. Chaudanson, G. Sitja, G. , and C. R. Henry, *Ultramicroscopy* **2006**, *106*, 503.
[4] P. L. Hansen, J. B. Wagner, S. Helveg, J. R. Rostrup-Nielsen, B. S. Clausen, H. Topsoe, *Science* **2002**, *295*, 2053.
[5] T. W. Hansen, J. B. Wagner, P. L. Hansen, S. Dahl, H. Topsoe, C. J. H. Jacobson, *Science* **2001**, *294*, 1508.
[6] P. A. Crozier, R. Sharma, A. K. Datye, *Microsc. Microanal.* **1998**, *4*, 278.
[7] P. A. Crozier, R. Wang, R. Sharma, *Ultramicroscopy* **2008**, *108*, 1432.
[8] P. Li, J. Liu, N. Nag, P. A. Crozier, *Appl. Catal. A* **2006**, *307*, 212.
[9] P. Li, J. Liu, N. Nag, P. A. Crozier, *J. Catal.* **2009**, *262*, 73.
[10] R. J. Liu, P. A. Crozier, C. M. Smith, D. A. Hucul, J. Blackson, G. Salaita, *Appl. Catal. A* **2005**, *282*, 111.
[11] V. P. Oleshko, P. A. Crozier, R. D. Cantrell, A. D. Westwood, *Macromol. Rapid Commun.* **2001**, *22*, 34. .
[12] R. Sharma, P. A. Crozier, Z. C. Kang, L. Eyring, *Philos. Mag.* **2004**, *84*, 2731.
[13] J. F. Creemer, S. Helveg, G. H. Hoveling, S. Ullmann, A. M. Molenbroek, P. M. Sarro, H. W. Zandbergen, *Ultramicroscopy* **2008**, *108*, 993.
[14] S. C. Tsang, J. B. Claridge, M. L.H Green, *Catal. Today* **1995**, *23*, 3.
[15] A. P. E. York, T. Xiao, M. L. H. Green, *Top. Catal.* **2003**, *22*, 345.
[16] J. X. Wang J. H. Lunsford, *J. Phys. Chem.* **1986**, *90*, 5883.
[17] M. A. Vannice, *Catal. Rev.* **1976**, *14*, 153.
[18] J. C. J. Bart, R. P. A. Sneeden, *Catal. Today* **1987**, *2*, 1.
[19] M. D. Cabezas, D. G. Lamas, M. G. Bellino, R. O. Fuentes, N. E. Walsoe de Reca, S. A. Larrondo, *Electrochem. Solid-State Lett.* **2009**, *12*, B34.
[20] P. D. F. Vernon, M. L. H. Green, A. K. Cheetham, A. T. Aschcroft, *Catal. Today* **1992**, *13*, 417.
[21] B. C. Enger, R. Lodeng, A. Holmen, *Appl. Catal. A* **2008**, *346*, 1.
[22] P. M. Torniainen, X. Chu, L. D. Schmidt, *J. Catal.* **1994**, *146*, 1.
[23] D. Dissanayake, M. P. Rosynek, Karl C. Kharas, Jack H. Lunsford, *J. Catal.* **1991**, *132*, 117.
[24] P. Li, J. Liu, N. Nag, P. A. Crozier, *J. Phys. Chem. B* **2005**, *109*, 13883.
[25] P. Li, J. Liu, N. Nag, P. A. Crozier, *Surf. Sci.* **2006**, *600*, 693.
[26] A. K. Datye, N. J. Long, *Ultramicroscopy* **1988**, *25*, 203.
[27] D. R. Gaskell, *Introduction to the Thermodynamics of Materials*, Taylor&-Francis, **2003**, p. 582.
[28] P. E. M. Siegbahn, U. Wahlgren, *Int. J. Quantum Chem.* **1992**, *42*, 1149.
[29] P. E. M. Siegbahn, I. Panas, *Surf. Sci.* **1990**, *240*, 37.
[30] A. D. Smigellkas, E. O. Kirkendall, *Trans. Am. Inst. Min. Metall. Pet. Eng.* **1947**, *171*, 130.
[31] A. Atkinson, D. P. Moon, D. W. Smart, R. I. Taylor, *J. Mater. Sci.* **1986**, *21*, 1747.
[32] A. Atkinson, R. I. Taylor, *J. Mater. Sci.* **1978**, *13*, 427.
[33] R. Peraldi, D. Monceau, B. Pieraggi, *Oxid. Met.* **2002**, *58*, 275.
[34] J. G. Railsback, A. C. Johnston-Peck, J. Wang, J. B. Tracy, *ACS Nano* **2010**, *4*, 1913.
[35] R. Nakamura, J. G. Lee, H. Mori, H. Nakajima, *Philos. Mag.* **2008**, *88*, 257.
[36] D. B. Williams, C. B. Carter, *Transmission Electron Microscopy Imaging III*, Springer, **1996**, p. 444.
[37] P. A. Crozier, A. K. Datye, *Stud. Surf. Sci. Catal.* **2000**, *130*, 3119.
[38] G. J. Lloyd, J. W. Martin, *Met. Sci. J.* **1972**, *6*, 7.
[39] W. Stober, A. Fink, E. Bohn, *J. Colloid Interface Sci.* **1968**, *26*, 62.
[40] R. Banerjee, S. Chenna, P. A. Crozier, *Microsc. Microanal.* **2009**, *15(Suppl 2)*, 732.
[41] C. H. Bartholomew, *Appl. Catal. A* **2001**, *212*, 17.

Received: July 10, 2010
Published online on ■■ ■■, 2010

*S. Chenna, R. Banerjee, P. A. Crozier**

■■ – ■■

Atomic-Scale Observation of the Ni Activation Process for Partial Oxidation of Methane Using In Situ Environmental TEM

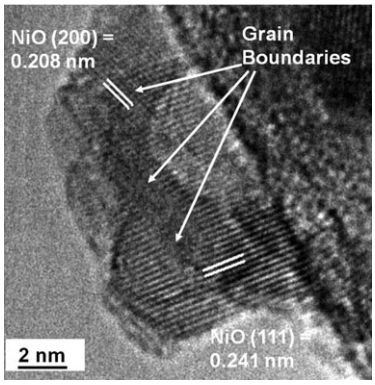

ETEM and smile: In situ environmental transmission electron microscopy (ETEM) is employed to develop an atomic-level understanding of the structure, composition, and morphologies that develop in a model Ni/SiO_2 catalyst during ramp-up for partial oxidation of methane under high-conversion conditions. Gas composition along the catalyst bed varies in space and time during the ramp-up.■■ok?■■

